

# Is the compact binary coalescence, GW190425, a strange quark star?

J. Sedaghat<sup>1\*</sup>, S. M. Zebarjad<sup>1,2†</sup>, G. H. Bordbar<sup>1,3‡</sup>, B. Eslam Panah<sup>4,5,6,7§</sup>, and R. Moradi<sup>6,7¶</sup>,

<sup>1</sup> Department of Physics, Shiraz University, Shiraz 71454, Iran

<sup>2</sup> Department of Physics, University of California at San Diego, La Jolla, CA 92093, USA

<sup>3</sup> Department of Physics and Astronomy, University of Waterloo,  
200 University Avenue West, Waterloo, Ontario N2L3G1, Canada

<sup>4</sup> Sciences Faculty, Department of Physics, University of Mazandaran, P. O. Box 47415-416, Babolsar, Iran

<sup>5</sup> ICRA-Net-Mazandaran, University of Mazandaran, P. O. Box 47415-416, Babolsar, Iran

<sup>6</sup> ICRA-Net, Piazza della Repubblica 10, I-65122 Pescara, Italy

<sup>7</sup> ICRA, Dipartimento di Fisica, Università di Roma “La Sapienza”, Piazzale Aldo Moro 5, I-00185 Roma, Italy

In this study, the effects of different QCD models in the structure of strange quark star (SQS) are investigated. In these models, the running coupling constant has a finite value in the infrared region of energy. By imposing some constraints on the strange quark matter (SQM) and by exploiting the analytic and background perturbation theories, the equations of states for the SQM are obtained. Then, the properties of SQSs in general relativity are evaluated. By using component masses of GW190425 [1] as well as some conversion relations between the baryonic mass and the gravitational mass, the remnant mass of GW190425 is obtained. Our results for the maximum gravitational mass of SQS are then compared with the remnant mass of GW190425. The results indicate that the obtained maximum gravitational masses are comparable to the remnant mass of GW190425. Therefore, it is proposed that the remnant mass of GW190425 might be a SQS.

## I. INTRODUCTION

Compact stars are considered as large laboratories for investigating quantum chromodynamics (QCD) models. One of the most challenging issues in QCD is the infrared (IR) scale behavior of the running coupling constant. The running coupling constant obtained from the renormalization procedure and the renormalization group equations has a well-defined behavior at large momenta [2, 3]. However, it becomes infinite at a point in IR scale called Landau pole ( $\Lambda$ ). Based on the perturbative QCD, the quark confinement originates from the Landau pole which depends on the selected renormalization scheme [4]. Nevertheless, the data extracted from some experiments indicate that the running coupling constant of QCD at low momenta is finite and freezes to a constant value [4]. For example, the effective strong coupling constant ( $\alpha_{s,g1}(Q^2)$ ) defined based on the Bjorken sum rule has been extracted from the CLAS spectrometer [5] where the polarized electron beam (with energies ranging from 1 to 6 GeV) collides with proton and deuteron targets. The data show that  $\alpha_{s,g1}(Q^2)$  loses its scale dependence at low momenta. In Ref. [6], by analyzing the energy spectra of heavy quark jets from  $e^+e^-$  annihilation, the IR value for the effective coupling constant ( $\alpha_s^{eff}(Q)$ ), is obtained as  $(2\text{GeV})^{-1} \int_0^{2\text{GeV}} (\alpha_s^{eff}(Q)/\pi) dQ = 0.18 \pm 0.01$ . Using the data of hadronic decays of the  $\tau$ -lepton ex-

tracted from the OPAL detector at LEP [7], it is shown that for a hypothetical  $\tau$ -lepton with the mass of  $m_{\tau'}$ , the effective charge  $\alpha_{\tau}(m_{\tau'}^2)$ , freezes at the mass scale of  $m_{\tau'}^2 \cong 1\text{GeV}^2$  with the magnitude of  $0.9 \pm 0.1$  [8]. Such behavior of the coupling constant at low momenta is called IR freezing in the literature. This effect can be explained by the running behavior of the coupling constant which stems from particle-antiparticle loop corrections. Due to confinement, quarks and antiquarks cannot have a wavelength larger than the size of the hadron. This suppresses the loop corrections at the IR scale. Consequently,  $\alpha_s$  is expected to lose its energy dependence at low energies [9]. In addition, the theoretical results from the Lattice QCD [10] and the Schwinger-Dyson framework [11], show that  $\alpha_s$  freezes at low momenta. There are other models such as the Stochastic quantization approach [12], the optimized perturbation theory [13], the Gribov-Zwanziger approach [14], and the background perturbation theory [15, 16], in all of which  $\alpha_s$  runs with an IR freezing effect. Moreover, the analytic perturbation theory presents a running coupling constant with a slowly varying behavior at low energies [17]. It should be noted that for the quark confinement, the coupling constant does not need to be infinite in the IR region. For example, the lattice simulations show that the  $q\bar{q}$  potential increases linearly at distances larger than  $0.4\text{fm}$ , while the coupling constant freezes at a maximum value [18]. Contrary to general belief, the value of the coupling constant does not need to be infinite in the IR region in order to confine light quarks [19].

In this paper, the IR behavior of the QCD running coupling constant in different models is first investigated. Then, two models are selected for the perturbative calculation of the equations of states (EOSs) of strange quark matter (SQM) in the leading order of  $\alpha_s$ . These two models are i) the analytic perturbation theory (APT)

\*J.sedaghat@shirazu.ac.ir

†zebarjad@shirazu.ac.ir

‡ghbordbar@shirazu.ac.ir

§eslamanah@umz.ac.ir

¶Rahim.Moradi@icranet.org

and ii) the background perturbation theory (BPT). Afterward, the EOSs are used in the TOV equation to calculate the maximum gravitational masses of strange quark stars (SQSs). Motivated by the LIGO detection of the compact binary coalescence (GW190425) with the total mass of  $3.4^{+0.3}_{-0.1} M_{\odot}$  [1], we compared our results with the remnant mass of GW190425. This binary is more massive than the other reported Galactic double neutron stars (NSs) [20]. Since no electromagnetic counterpart has been observed for GW190425, its origin is unknown [21]. Various models have suggested the nature of GW190425. In Ref. [21], the possibility whether GW190425 is a binary NS merger or a black hole-NS (BH-NS) merger has been investigated. It is hypothesized that the progenitor of GW190425 is a binary including a NS and a  $4 - 5 M_{\odot}$  helium star [22]. Furthermore, it is suggested that GW190425 is a NS-BH merger with the masses of  $1.15^{+0.15}_{-0.13} M_{\odot}$  and  $2.4^{+0.36}_{-0.32} M_{\odot}$  for the NS and the BH, respectively [23]. In addition, using a toy model, some researchers have investigated whether future LISA observations could detect binary NSs like GW190425 [24]. In Ref. [25], GW190425 and GW190814 have been investigated as primordial BH clusters. In this paper, it is not intended to probe the nature of GW190425. Rather, the aim is to explore whether the remnant mass of GW190425 is a SQS. In this study, it is shown that the maximum gravitational masses of SQSs are comparable with the remnant mass of GW190425.

## II. IR BEHAVIOR OF $\alpha_s$ IN DIFFERENT MODELS

As was discussed above, there are experimental evidence and models which support the slowly varying or freezing behavior of the running coupling constant in the IR region. However, there is no consensus on the freezing point and the corresponding value of the coupling constant. In this section, the running coupling constant behaviors of different QCD models in the IR  $Q^2$  are investigated. These models are as follows: i) regular perturbation theory (RPT); ii) APT; iii) BPT; iv) flux-tube model (FTM) [26]; and v) Cornwall Schwinger-Dyson equation (CSD) [27]. The behavior of the running coupling constant in these models for  $Q < 3\text{GeV}$  is shown in Figure 1. According to this figure, as  $Q$  decreases in the IR region,  $\alpha_{RPT}$  varies much more slowly than  $\alpha_{RPT}$ . Nevertheless, compared to the other models,  $\alpha_{RPT}$  increases faster in the IR region, especially for  $Q < 0.7$  GeV. The couplings of the BPT, FTM, and CSD models have a very slowly varying behavior in the IR momenta so that it can be said that they freeze compared to the couplings of RPT and APT. However, for ultraviolet (UV) momenta, all the models have an asymptotic behavior and coincide with each other. Two of the mentioned coupling constants (except for that of RPT) with higher values in the IR region are used. After a brief description of these models, they are used to calculate the perturbative EOSs

of SQM. The models are as follows:

1) APT: The analytic coupling constant ( $\alpha_{an}$ ) at one-loop approximation [17] is derived in Appendix A as

$$\alpha_{APT}^{(1)}(Q^2) = 4\pi/\beta_0 \left[ \left( \ln \left( \frac{Q^2}{\Lambda^2} \right) \right)^{-1} + \frac{\Lambda^2}{\Lambda^2 - Q^2} \right]. \quad (1)$$

Supposing that  $N_c$  and  $N_f$  are the number of colors and flavors respectively,  $\beta_0$  is defined as  $\frac{11N_c - 2N_f}{3}$ . It can be seen that this running coupling constant has  $Q^2$  analyticity at all points and decreases monotonously in the IR region without any divergence [4]. The interesting feature of this running coupling is that  $\alpha_{an}(Q^2 = 0) = 4\pi/\beta_0$  has no dependence on the QCD scale parameter ( $\Lambda$ ). Furthermore, all perturbative orders of  $\alpha_{an}$  have the same value at  $Q^2 = 0$ . Hence, it is expected that different orders of  $\alpha_{an}(Q^2)$  have close values. For example, in the  $\overline{MS}$  modified minimal subtraction scheme,  $\alpha_{an}^{(1)}(Q^2)$  and  $\alpha_{an}^{(2)}(Q^2)$  differ within the 10% interval and  $\alpha_{an}^{(2)}(Q^2)$  and  $\alpha_{an}^{(3)}(Q^2)$  differ within the 1% interval [17].

2) BPT: The running coupling constant in the framework of the BPT is given by

$$\alpha_{BPT}^{(1)}(Q^2) = \frac{4\pi}{\beta_0} \left( \ln \left[ (Q^2 + m_{2g}^2)/\Lambda^2 \right] \right)^{-1}, \quad (2)$$

where  $m_{2g}^2$  is the mass of two gluons connected by the fundamental string ( $\sigma$ ). This effective mass is added to the logarithm argument to avoid the  $\Lambda$  pole problem (see Appendix B for more details). In the  $q\bar{q}$  potential [28],  $m_{2g}^2 = 2\pi\sigma \approx 1\text{GeV}$  [16, 29].

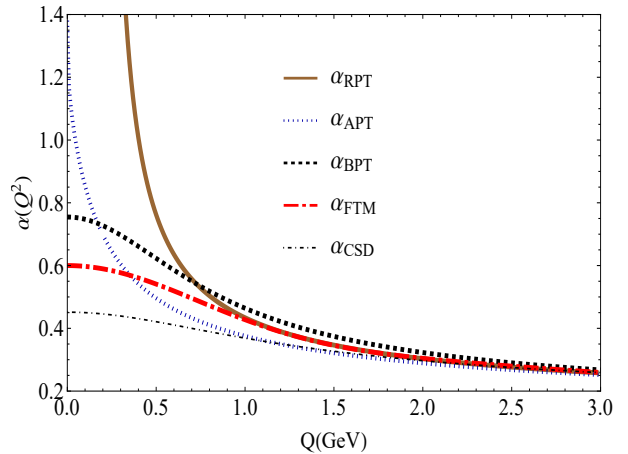


FIG. 1: QCD running coupling constant versus renormalization scale for different models.

### A. Thermodynamic potential

The system under study is the SQM composed of up, down, and strange quark flavors at zero temperature and

finite chemical potential. The masses of the up and down quarks are negligible. However, for the strange quark, the running mass with the value of  $0.95^{+9}_{-3}\text{MeV} \cong 0.1\text{GeV}$  in  $Q = 2\text{GeV}$  [30] is considered. Since the QED interactions between quarks and the interactions between gravitons are negligible compared to the QCD interaction, QCD is the dominant interaction in the system. By knowing the thermodynamic potential of the system, the properties of the SQM such as energy density, quark number density, pressure, sound speed, adiabatic index, etc. can be derived. To obtain the thermodynamic potential ( $\Omega$ ), it is divided into non-interacting and perturbative parts: i) the non-interacting or free part consists of non-interacting quarks and electrons; ii) the perturbative part consists of the QCD interactions between the quarks. The perturbative part has been previously obtained through two- and three-loop Feynman diagrams up to the first and second order of the coupling constant, in Refs. [31] and [32], respectively. The pressure is derived from the relation  $P = -B - \frac{\Omega}{V}$ , where  $V$  is the volume of the system. It is notable that  $B$  is a free parameter considered for all non-perturbative effects not included in the perturbative expansion [32]. In fact, if the perturbative interaction between the quarks is neglected,  $B$  will have the role of the bag constant in the system. The renormalization scale  $Q$  appears in pressure through the running mass of the strange quark and the running coupling constant. At finite temperature ( $T$ ) and finite chemical potential ( $\mu$ ), the phenomenological models suggest  $Q = 2\pi\sqrt{T^2 + \frac{\mu^2}{\pi^2}}$  for a massless quark. At zero temperature with  $N_f$ ,  $Q = 2\left(\sum_f \mu_f/3\right) \equiv 2\bar{\mu}$  which can vary by a factor of 2 with respect to its central value [33–35]. First, the minimum allowed value for the renormalization scale in which the strange quark number density is non-zero is obtained. Afterward, using the constraint of the stars moment of inertia, the maximum allowed value for the renormalization scale is obtained. In fact, it has been shown that for non-rotating (NR) or slowly-rotating (SR) stars, the normalized moment of inertia ( $I/(MR^2)$ ) increases as the compactness ( $M/R$ ) of the star increases [36, 37]. For the applied models in this paper, the range  $2.8\bar{\mu} < Q < 3.4\bar{\mu}$  satisfies all the required constraints in SQS.

## B. Stability conditions and EOSs

After calculating the thermodynamic potential, the EOSs of the stable SQSs can be obtained from the following relation

$$\varepsilon = -(P_u + P_d + P_s) + \mu_u n_u + \mu_d n_d + \mu_s n_s, \quad (3)$$

where  $\varepsilon$ ,  $P_i$ ,  $\mu_i$  and  $n_i$  are the energy density, pressure, chemical potential, and quark number density with flavor  $i$ , respectively. It should be noted that to calculate the EOSs, the charge neutrality and beta equilibrium constraints have to be imposed [38]. As a result,

$\mu_s = \mu_d \equiv \mu$ ,  $\mu_u = \mu - \mu_e$ , and  $2n_u/3 - n_d/3 - n_s/3 - n_e = 0$  hold where  $n_e = eB\mu_e^2/(2\pi)^2$  is the electron number density. Another constraint is that the minimum energy density per baryon number density should be lower than that of the most stable nucleus ( $^{56}\text{Fe}$ ) [39–41], i.e.  $\varepsilon/n_B \leq 0.93\text{GeV}$  where  $n_B$  is the baryon number density and is equals  $n_B = (n_u + n_d + n_s)/3$ . The minimum value of  $n_B$  corresponds to the point that the strange quark number density is non-zero provided that the constraint for the minimum energy density per baryon is satisfied and the perturbative expansions of the pressures and the quark number densities are not broken down.

## C. Thermodynamic properties of SQM in BPT and APT models

Here, the results for the EOSs of SQM in the APT and BPT models are presented. First, the critical baryon number density ( $n_{cr}$ ) at which SQM begins to appear should be obtained. For this purpose, the minimum value of  $n_B$  is calculated. For this value, the perturbative expansion must be valid and the constraints of the SQM must be satisfied. The selected baryon number density is referred to as the minimum critical baryon number density and is denoted by  $(n_{cr})_{min}$ . The value of  $n_{cr}$  must be more than  $(n_{cr})_{min}$  because the higher order contributions (compared with the leading order) in the perturbative expansion are ignored. Table. I, shows the values of  $(n_{cr})_{min}$  in the RPT, APT and BPT models for different values of the renormalization scale. As one can see from Table. I, the  $(n_{cr})_{min}$  of the APT and BPT models is obtained at lower energies than that of the RPT model. This feature is due to the behavior modification of the coupling constant in the IR region in the APT and BPT models. Moreover, there is little difference between the  $(n_{cr})_{min}$  values of the APT and BPT models. This stems from the fact that the  $(n_{cr})_{min}$  values are obtained at  $Q \gtrsim 0.8\text{GeV}$  where the coupling constants in the APT and BPT models behave almost similarly (see Figure. 1). According to Table. I, the value of  $(n_{cr})_{min}$  for the APT and BPT models is about  $0.1\text{fm}^{-3}$ . As was mentioned above,  $n_{cr} > (n_{cr})_{min}$  values must be used. Using bag models in Refs. [42] and [43],  $n_{cr}$  was obtained in the interval  $0.1\text{fm}^{-3} \lesssim n_{cr} \lesssim 0.5\text{fm}^{-3}$ . By setting  $Q = 3.4\bar{\mu}$ , different values of  $n_{cr} \geq (n_{cr})_{min}$  are selected to obtain EOSs and consequently the maximum gravitational masses of SQSs in the APT and BPT models. It is noteworthy that the maximum gravitational masses are decreased by increasing  $n_{cr}$ .

In Figure. 2, the EOSs of SQM in the APT and BPT models are presented for different values of  $n_{cr}$ . Each color corresponds to a different  $n_{cr}$ . In both models, the EOSs become softer when  $n_{cr}$  increases.

It is worthwhile to mention that the EOSs should satisfy the conditions of causality and dynamic stability. To meet the causality condition, the speed of sound ( $c_s = \sqrt{dP/d\varepsilon}$ ) should be lower than the speed of light

TABLE I: Minimum values of baryon number density  $(n_{cr})_{min}$  for the phase transition from baryon matter to quark matter by considering different values of renormalization scales in various models.

$\frac{Q}{\mu}$	<i>RPT</i>		<i>APT</i>		<i>BPT</i>	
	$\bar{\mu}$ (MeV)	$(n_{cr})_{min}$ ( $fm^{-3}$ )	$\bar{\mu}$ (MeV)	$(n_{cr})_{min}$ ( $fm^{-3}$ )	$\bar{\mu}$ (MeV)	$(n_{cr})_{min}$ ( $fm^{-3}$ )
2.8	303	0.196	244	0.109	258	0.098
3.1	292	0.179	241	0.106	252	0.097
3.4	281	0.162	237	0.101	248	0.096

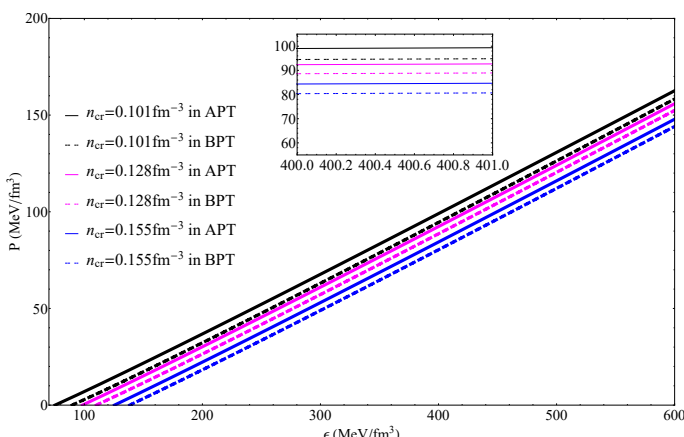


FIG. 2: EOSs of SQM in APT and BPT models for different choices of  $n_{cr}$ . Continuous and dashed lines correspond to APT and BPT models, respectively. Each color indicates a  $n_{cr}$  as follows. Continuous and dashed black lines correspond to  $n_{cr} = 0.101 fm^{-3}$ , continuous and dashed magenta lines correspond to  $n_{cr} = 0.128 fm^{-3}$ , and continuous and dashed blue lines correspond to  $n_{cr} = 0.155 fm^{-3}$ .

in vacuum ( $c_s \leq 1$ ). Figure. 3, shows the behavior of  $c_s^2$  versus energy density for different values of  $n_{cr}$ . Based on some arguments in the perturbation theory,  $c_s^2$  should approach  $1/3$  from below at asymptotically large densities [44]. Figure. 3, indicates that this behavior is well satisfied in our EOSs for both APT and BPT models.

To satisfy the dynamic stability condition, the value of the adiabatic index  $(\Gamma = \frac{(P+\epsilon)dP}{Pd\epsilon})$  should be higher than  $4/3$  [45–50]. This constraint holds for our EOSs in both APT and BPT models. Figure. 4, shows that the adiabatic index of SQM versus energy density is higher than  $4/3$  for all  $n_{cr}$  values used in both APT and BPT models. It is worth mentioning that the constraints  $\epsilon + P \geq 0$  and  $\epsilon \geq |P|$  [51–54] are well satisfied in our calculations as well.

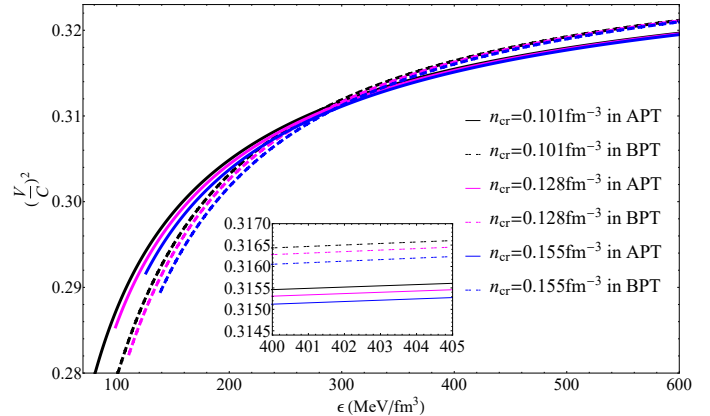


FIG. 3: Squared sound velocity versus energy density in APT and BPT models for different choices of  $n_{cr}$ . Continuous and dashed lines correspond to APT and BPT models, respectively. Each color indicates a  $n_{cr}$  as follows. Continuous and dashed black lines correspond to  $n_{cr} = 0.101 fm^{-3}$ , continuous and dashed magenta lines correspond to  $n_{cr} = 0.128 fm^{-3}$ , and continuous and dashed blue lines correspond to  $n_{cr} = 0.155 fm^{-3}$ .

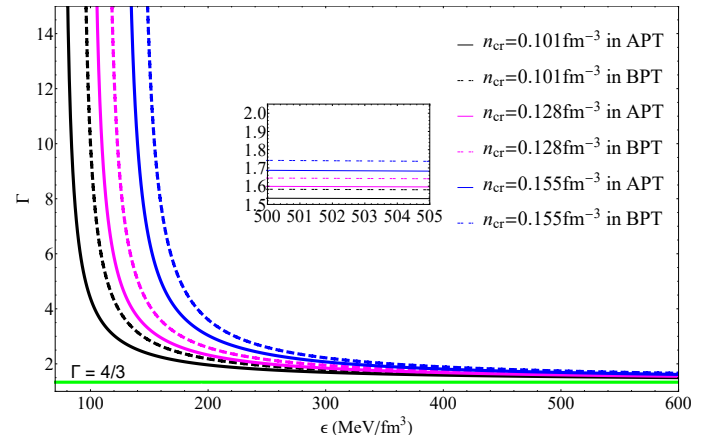


FIG. 4: Adiabatic index in APT and BPT models for different choices of  $n_{cr}$ . Continuous and dashed lines correspond to APT and BPT models, respectively. Each color indicates a  $n_{cr}$  as follows. Continuous and dashed black lines correspond to  $n_{cr} = 0.101 fm^{-3}$ , continuous and dashed magenta lines correspond to  $n_{cr} = 0.128 fm^{-3}$ , and continuous and dashed blue lines correspond to  $n_{cr} = 0.155 fm^{-3}$ .

#### D. Calculation of the remnant masses of non-rotating and rapidly-rotating compact stars

The gravitational wave (GW) observations give the total gravitational mass of the binary system with the assumption that its components are in an infinite distance from each other [55]. In order to obtain the remnant mass of a binary NS merger, the total baryonic mass must first be calculated from the total gravitational mass through

the conversion relations shown in Table. II [55–58]. As one can see from Table. II, there are some conversion relations between baryonic mass ( $M_b$ ) and gravitational mass ( $M_g$ ) for NR and rapidly rotating (RR) NSs. After calculating the total baryonic mass from components of the binary, the mass ejected during the merger is deduced from it. Hence, the remnant baryonic mass is obtained and converted back to the remnant gravitational mass. Before the merger, the low-spin approximation is assumed for the components in the binary system. Therefore, the conversion relations are used for NR stars. There is a different scenario for the remnant mass. Since the remnant mass must be rapidly spinning, the RR conversion relations between  $M_b$  and  $M_g$  are used [55]. The first and last relations in Table. II are used as the conversion relations for the phases before and after the merger, respectively. Assuming the maximum expected value of the mass ejected for GW190425 ( $M_{ejecta} = 0.04M_\odot$  [59]), the remnant mass of GW190425 is obtained in the range of  $3.11 - 3.54M_\odot$ . It should be noted that in the calculations, the mass ratio of the binary GW190425 is bound to  $0.4 - 1$  [1].

TABLE II: Relation between total baryonic mass and total gravitational mass for NR and RR stars. Below each relation, there are two numbers as the maximum residual error (outside the parenthesis) and the average residual error (inside the parenthesis).

NR NSs	RR NSs
$M_b = Mg + 0.075M_g^2$ 5.8%(1.5%) [57]	$M_b = Mg + 0.064M_g^2$ 3.3%(1.2%) [55]
$M_b = Mg + 0.084M_g^2$ 4.1%(1.7%) [56]	$M_b = Mg + 0.073M_g^2$ 6.0%(1.6%) [55]
$\frac{M_b}{M_g} = 1 + 0.89\left(\frac{M_g}{R}\right)^{1.2}$ 2.6%(0.56%) [58]	$M_b = Mg + 0.056M_g^2 + 0.002M_g^3$ 4.0%(0.95%) [55]

### III. SQS STRUCTURE

Using the computed EOSs in section C, the maximum gravitational mass can be obtained by solving the TOV equation [60, 61]. The results for the APT and BPT models have been presented in Tables. III, and IV and Figure. 5. In Ref. [32], the maximum gravitational mass of SQS has been obtained as  $M \simeq 2.75M_\odot$  by using the RPT model. Our results in the APT model for  $(n_{cr})_{min} = 0.101\text{fm}^{-3}$  and  $n_{cr} = 0.128\text{fm}^{-3}$  are considerably larger than that in [32]. This indicates the great importance of the IR behavior of the running coupling constant in the structure of a quark star. There are different colored regions in Figure. 5. The blue region shows the remnant mass of GW190425 obtained in section D. In

TABLE III: The properties of the NR and RR SQSs in the APT model for different values of  $n_{cr}$ . It is notable that indices NR and RR, are related to NR and RR SQSs.

$n_{cr}$ $\text{fm}^{-3}$	$M_{max_{NR}}$ $(M_\odot)$	$R_{NR}$ $(\text{km})$	$M_{max_{RR}}$ $(M_\odot)$	$M_{B_{NR}}$ $(M_\odot)$	$R_{Sch_{NR}}$ $(\text{km})$	$z_{NR}$
0.101	3.16	17.74	3.79	5.35	9.32	0.45
0.128	2.88	16.14	3.46	4.87	8.50	0.45
0.155	2.57	14.45	3.08	4.36	7.58	0.45

TABLE IV: The properties of the NR and RR SQSs in the BPT model for different values of  $n_{cr}$ .

$n_{cr}$ $\text{fm}^{-3}$	$M_{max_{NR}}$ $(M_\odot)$	$R_{NR}$ $(\text{km})$	$M_{max_{RR}}$ $(M_\odot)$	$M_{B_{NR}}$ $(M_\odot)$	$R_{Sch_{NR}}$ $(\text{km})$	$z_{NR}$
0.101	3.00	17.00	3.60	5.13	8.84	0.44
0.128	2.72	15.12	3.26	4.56	8.02	0.45
0.155	2.45	13.86	2.94	4.18	7.22	0.44

the current study, the maximum gravitational mass for the RR SQS represented by the horizontal green region ranged from  $2.94$  to  $3.79 M_\odot$ . The vertical green region which represents the corresponding radius of the maximum mass of the RR SQSs ranged from  $13.86 \text{ Km}$  to  $17.74 \text{ Km}$  in our calculations. Finally, the black hatched region, which is the common region between the two mentioned green regions, shows our results for the RR SQSs. As can be observed in Fig. 5, this region completely covers the remnant mass of GW190425.

Now, it is explained how to calculate the maximum gravitational masses of the RR SQSs in the APT and BPT models. As was mentioned in section D, the remnant mass must be rapidly-rotating. If the rapidly-rotating remnant mass loses its centrifugal support, it will collapse into a BH [62]. To obtain the maximum mass of the rotating SQSs, the universal relations derived in Ref. [37] were used. The authors used 15 nuclear-physics EOSs for NR, SR and RR compact stars and obtained a universal relation between the critical (maximum) mass which has a uniform rotation and the maximum mass of the NR star ( $M_{TOV}$ )

$$M_{crit} = M_{TOV} \left( 1 + a_1 \left( \frac{j}{j_{Kep}} \right)^2 + a_2 \left( \frac{j}{j_{Kep}} \right)^4 \right), \quad (4)$$

where  $a_1 = 1.316 \times 10^{-1}$ ,  $a_2 = 7.111 \times 10^{-2}$ , and  $j = \frac{J}{M^2}$  is the dimensionless angular momentum in which  $J$  and  $M$  are the angular momentum and the mass of the star, respectively. In addition,  $j_{Kep}$  is  $\frac{J_{Kep}}{M_{Kep}^2}$ , where  $J_{Kep}$  is the Keplerian angular momentum (the maximum achievable angular momentum) and  $M_{Kep}$  is the maximum mass of the star. Substituting  $j$  with  $j_{Kep}$  in Eq. 4, the maximum mass of the rotating star is obtained

$$M_{max} = (1.203 \pm 0.022)M_{TOV}. \quad (5)$$

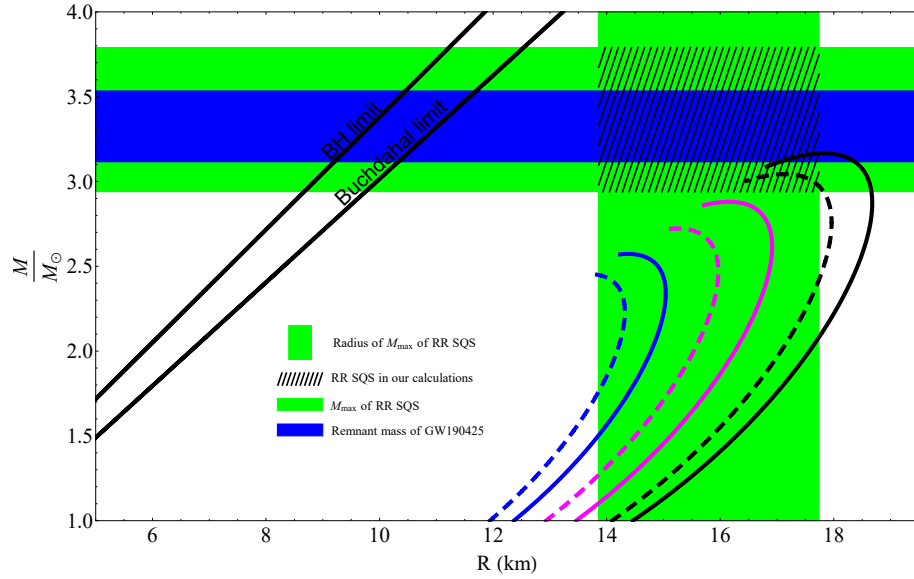


FIG. 5:  $M$ - $R$  of SQSs in the APT and BPT models for different choices of  $n_{cr}$ . The blue region is related to the remnant mass of GW190425. The horizontal and vertical green regions show intervals of maximum mass of RR SQSs and corresponding radii, respectively. The black hatched region is related to our results for maximum masses and corresponding radii of RR SQSs. Continuous and dashed lines correspond to different  $n_{cr}$ , which are the same as the ones in Figures. 2, 3 and 4.

The result is a horizontal green region in Figure. 5, which ranges from  $2.94$  to  $3.79 M_{\odot}$ .

It has previously been shown that when the causality and Le Chatelier principles are used in GR, the mass of a NS cannot be larger than  $3.2M_{\odot}$  [63]. Therefore, the remnant mass of GW190425 is not expected to be a NS. Moreover, the upper mass limit of a static spherical star with a uniform density in GR is given by  $M_B = \frac{4c^2 R}{9G}$  (the Buchdahl theorem) [64]. According to this compactness limit, a boundary between a BH and a star can be determined. Indeed, for  $M_{max} < M_B$ , the compact object cannot be a BH. In other words, the results show that the maximum masses of the compact objects in the current study are less than the mass of the Buchdahl limit. Hence, these massive compact objects are not BHs (see Tables. III and IV). In addition, the radii of these compact objects are more than the Schwarzschild radius ( $R > R_{Sch} = \frac{2GM}{c^2}$ ) and the obtained redshifts are less than 1  $\left( z = \frac{1}{\sqrt{1 - \frac{2GM}{c^2 R}}} - 1 < 1 \right)$  (see Tables . III and

IV). These results ensure that these compact objects are not BHs or NSs. As a result, RR SQSs may have masses larger than  $3.2M_{\odot}$ . Therefore, the remnant mass of GW190425 may be considered as a SQS.

#### IV. SUMMARY AND CONCLUSION

In this paper, the EOSs of SQSs were calculated using the APT and BPT models. It is known that the coupling

constant behavior of the QCD is a challenging issue. Unlike the RPT model in which the coupling constant is infinite at IR momenta, the employed models in this paper presented a finite running coupling constant at all energy scales. Considering compact stars as large laboratories to probe the QCD models, the EOSs in GR were used in order to investigate the structural properties of SQSs at zero temperature. In this study, the maximum gravitational masses were considerably larger than that of the RPT. By using the component masses of GW190425 as well as some conversion relations between the baryonic mass and the gravitational mass, the remnant mass of GW190425 was obtained. Our results for the maximum gravitational mass of SQSs were comparable with the remnant mass of GW190425. Then, the obtained gravitational masses were modified by considering the effect of the rotation of the star on them. In this way, the results completely covered the remnant mass of GW190425 and showed that the remnant mass of GW190425 might be a SQS.

#### Acknowledgements

We are indebted to Prof. Yu. A. Simonov and Prof. Luciano Rezzolla for their fruitful comments and discussions on the background perturbation theory and the maximum mass of rotating compact objects, respectively. SMZ and GHB thank the Research Council of Shiraz University. SMZ thanks the Physics Department of UCSD for their hospitality during his sabbatical. BEP thanks

University of Mazandaran. The work of BEP has been supported by University of Mazandaran by title "Evolu-

tion of the masses of celestial compact objects in various gravity".

---

[1] B. P. Abbott, et al., *Astrophys. J. Lett.* **892**, L3 (2020).  
[2] G. M. Prosperi, M. Raciti, and C. Simolo, *Prog. Part. Nucl. Phys.* **58**, 387 (2007).  
[3] G. Altarelli, [arXiv:1303.6065].  
[4] A. Deur, S. J. Brodsky, and G. F. de Teramond, *Prog. Part. Nucl. Phys.* **90**, 1 (2016).  
[5] A. Deur, V. Burkert, J. P. Chen, and W. Korsch, *Phys. Lett. B* **665**, 349 (2008).  
[6] R. Perez-Ramos, V. Mathieu, and M. -A. Sanchis-Lozano, *JHEP* **10**, 47 (2010).  
[7] OPAL Collaboration, *Euro. Phys. J. C* **7**, 571 (1999).  
[8] S. J. Brodsky, S. Menke, C. Merino, and J. Rathsman, *Phys. Rev. D* **67**, 055008 (2003).  
[9] S. J. Brodsky, and R. Shrock, *Phys. Lett. B* **666**, 95 (2008).  
[10] G. S. Bali, *Phys. Rep.* **343**, 1 (2001).  
[11] C. S. Fischer, *J. Phys. G Nucl. Phys.* **32**, R253 (2006).  
[12] D. Zwanziger, *Phys. Rev. D* **65**, 094039 (2002).  
[13] A. C. Mattingly, and P. M. Stevenson, *Phys. Rev. Lett.* **69**, 1320 (1992).  
[14] J. A. Gracey, *JHEP* **06**, 052 (2006).  
[15] A. M. Badalian, and Yu. A. Simonov, *Phys. At. Nucl.* **60**, 630 (1997).  
[16] Yu. A. Simonov, *Phys. At. Nucl.* **74**, 1223 (2011).  
[17] D. V. Shirkov, and I. L. Solovtsov, *Phys. Rev. Lett.* **79**, 1209 (1997).  
[18] G. S. Bali, et al., *Nucl. Phys. B Proc. Suppl.* **153**, 9 (2006).  
[19] V. Gribov, *Euro. Phys. J. C* **10**, 71 (1999).  
[20] N. Farrow, X. -J. Zhu, and E. Thrane, *Astrophys. J.* **876**, 18 (2019).  
[21] K. Kyutoku et al., *Astrophys. J. Lett.* **890**, L4 (2020).  
[22] I. M. Romero-Shaw, N. Farrow, S. Stevenson, E. Thrane, and X. -J. Zhu, *MNRAS. Lett.* **496**, L64 (2020).  
[23] M. -Z. Han et al., *Astrophys. J. Lett.* **891**, L5 (2020).  
[24] V. Korol, and M. Safarzadeh, *MNRAS* **502**, 5576 (2021).  
[25] S. Clesse, and J. Garcia-Bellido, [arXiv:2007.06481].  
[26] S. Godfrey, and N. Isgur, *Phys. Rev. D* **32**, 189 (1985).  
[27] J. M. Cornwall, *Phys. Rev. D* **26**, 1453 (1982).  
[28] Yu. A. Simonov, *Phys. At. Nucl.* **58**, 107 (1995).  
[29] A. M. Badalian, and B. L. G. Bakker, *Phys. Rev. D* **100**, 054036 (2019).  
[30] P. A. Zyla et al. (Particle Data Group), *Prog. Theor. Exp. Phys.* **2020**, 083C01 (2020).  
[31] E. S. Fraga, *Nucl. Phys. A* **774**, 819 (2006).  
[32] A. Kurkela, P. Romatschke, and A. Vuorinen, *Phys. Rev. D* **81**, 105021 (2010).  
[33] R. A. Schneider, [arXiv:hep-ph/0303104].  
[34] B. Karmakar, R. Ghosh, A. Bandyopadhyay, N. Haque, and M. G. Mustafa, *Phys. Rev. D* **99**, 094002 (2019).  
[35] A. Bandyopadhyay, B. Karmakar, N. Haque, and M. G. Mustafa, *Phys. Rev. D* **100**, 034031 (2019).  
[36] A. Worley, P. G. Krastev, and B. -A. Li, *Astrophys. J.* **685**, 390 (2008).  
[37] C. Breu, and L. Rezzolla, *MNRAS* **459**, 646 (2016).  
[38] D. Blaschke, N. K. Glendenning, and A. Sedrakian, (Ed.), *Physics of neutron star interiors*, Germany: Springer (2001).  
[39] E. Witten, *Phys. Rev. D* **30**, 272 (1984).  
[40] H. Terazawa, *J. Phys. Soc. Jpn.* **58**, 3555 (1989).  
[41] F. Weber, *Prog. Part. Nucl. Phys.* **54**, 193 (2005).  
[42] I. Sagert et al., *Phys. Rev. Lett.* **102**, 081101 (2009).  
[43] I. Sagert et al., *J. Phys. G: Nucl. Part. Phys.* **37**, 094064 (2010).  
[44] H. Tan, J. Noronha-Hostler, and N. Yunes, *Phys. Rev. Lett.* **125**, 261104 (2020).  
[45] S. Chandrasekhar, *Astrophys. J.* **140**, 417 (1964).  
[46] J. M. Bardeen, K. S. Thorne, and D. W. Meltzer, *Astrophys. J.* **145**, 505 (1966).  
[47] H. Kuntsem, *MNRAS* **232**, 163 (1988).  
[48] M. K. Mak, and T. Harko, *Eur. Phys. J. C* **73**, 2585 (2013).  
[49] B. Eslam Panah et al., *Astrophys. J.* **848**, 24 (2017).  
[50] B. Eslam Panah, T. Yazdizadeh, and G. H. Bordbar, *Eur. Phys. J. C* **79**, 815 (2019).  
[51] S. H. Hendi, G. H. Bordbar, B. Eslam Panah, and S. Panahiyan, *JCAP* **09**, 013 (2016).  
[52] S. H. Hendi, G. H. Bordbar, B. Eslam Panah, and S. Panahiyan, *JCAP* **07**, 004 (2017).  
[53] B. Eslam Panah, and H. L. Liu, *Phys. Rev. D* **99**, 104074 (2019).  
[54] Z. Roupas, G. Panotopoulos, and I. Lopes, *Phys. Rev. D* **103**, 083015 (2021).  
[55] H. Gao et al., *Front. Phys.* **15**, 24603 (2020).  
[56] J. M. Lattimer, and A. Yahil, *Astrophys. J.* **340**, 426 (1989).  
[57] F. X. Timmes, S. E. Woosley, T. A. Weaver, *Astrophys. J.* **457**, 834 (1996).  
[58] M. Coughlin et al., *Astrophys. J.* **849**, 12 (2017).  
[59] R. J. Foley et al., *MNRAS* **494**, 190 (2020).  
[60] R. C. Tolman, *Phys. Rev.* **55**, 364 (1939).  
[61] J. R. Oppenheimer, and G. M. Volkoff, *Phys. Rev.* **55**, 374 (1939).  
[62] N. Sarin, P. D. Lasky, and G. Ashton, *Phys. Rev. D* **101**, 063021 (2020).  
[63] C. E. Rhoades, and R. Ruffini, *Phys. Rev. Lett.* **32**, 324 (1974).  
[64] H. A. Buchdahl, *Phys. Rev.* **116**, 1027 (1959).

### Appendix A: Deriving the analytic coupling constant at one-loop approximation

Using the Källén-Lehman spectral representation, the analytic coupling constant ( $\alpha_{an}$ ) is defined as [17]

$$\alpha_{APT} = \frac{1}{\pi} \int_0^\infty d\sigma \frac{\rho(\sigma, a)}{\sigma + Q^2 - i\epsilon}, \quad (6)$$

where  $\rho(\sigma, a) = \text{Im}(\alpha_{RG}(-\sigma - i\epsilon, a))$  is the spectral density function calculated by the imaginary part of  $\alpha_{RG}$  (the running coupling constant obtained from the renormalization group equations). The spectral density func-

tion at one-loop approximation is given by

$$\rho(\sigma, a) = \frac{a^2 \beta_0 \pi}{(1 + a\beta_0 \ln \sigma / \mu^2)^2 + (a\beta_0 \pi)^2}. \quad (7)$$

By inserting Eq. (7) in Eq. (6), we get

$$\alpha_{APT}^{(1)} = \frac{4\pi}{\beta_0} \left[ \left( \ln \left( \frac{Q^2}{\Lambda^2} \right) \right)^{-1} + \frac{\Lambda^2}{\Lambda^2 - Q^2} \right]. \quad (8)$$

## Appendix B: The running coupling constant in BPT

The running coupling constant derived from BPT [15, 16, 28] is based on the success of static potential  $q\bar{q}$  in which the QCD interaction is divided into two parts as  $V(r) = -\frac{4\alpha_V}{3r} + \sigma r$ . In this equation, the first term is the perturbative part for short-distance interactions and the second term is the non-perturbative part

for the long-distance interactions. In the BPT model, the gluon field is divided into perturbative and non-perturbative parts. The non-perturbative part is a background field which is described by the QCD string tension ( $\sigma$ ). To avoid the  $\Lambda$  pole problem, an effective gluonic mass ( $m_{2g}^2 = 2\pi\sigma$ ) is assumed to be produced by this non-perturbative background field [16]. The IR behavior of the running coupling constant is then modified by adding this non-perturbative part to all gluonic logarithms ( $\ln Q^2 \mapsto \ln(Q^2 + m_{2g}^2)$ ) at all loop orders. At one-loop approximation, the following equation is obtained

$$\alpha_{BPT}^{(1)}(Q^2) = \frac{4\pi}{\beta_0} \left( \ln \left( \frac{Q^2 + m_{2g}^2}{\Lambda^2} \right) \right)^{-1},$$

where,  $\Lambda$  is 0.480 GeV.